Improved Nonlinear Flux Observer-Based Second-Order SOIFO for PMSM Sensorless Control

Wei Xu, *Senior Member, IEEE*, Yajie Jiang, Chaoxu Mu, *Member, IEEE*, and Frede Blaabjerg, *Fellow, IEEE*

***Abstract*—The conventional rotor flux estimation method has issues of dc offset and harmonics, which are caused by initial rotor flux, detection errors, etc. To eliminate these defects, one improved nonlinear flux observer is proposed for sensorless control of permanent magnet synchronous machine (PMSM). First, the rotor position estimation method based on PMSM rotor flux observation is studied. Meanwhile, the limitations of the traditional rotor flux estimators, i.e., the saturation of pure integrator, phase shift, and amplitude attenuation of a low-pass filter are analyzed. Then, two novel flux observers, second-order generalized integral flux observer (SOIFO) and second-order SOIFO, are designed for the rotor flux estimation of PMSM. Based on second-order generalized integrator (SOGI) structure, the SOIFO can limit the dc component to a certain value. Furthermore, the second-order SOIFO is developed from the SOGI, which is characterized with effective dc and harmonics attenuation capability. With the second-order SOIFO, even without magnitude and phase compensation, the dc offset and harmonics of estimated rotor flux could be well eliminated. Therefore, the speed and rotor position can be estimated accurately. All the performances of the four methods are analyzed by transfer functions and Bode diagrams. Finally, the new sensorless control strategy is validated by comprehensive experimental results.**

***Index Terms*—Permanent magnet synchronous machine (PMSM), rotor flux estimation, second-order generalized integral flux observer (SOIFO), sensorless control.**

NOMENCLATURE

PMSM	Permanent magnet synchronous machine.
FOC	Field-orientation control.
EMF	Electromotive force.

Manuscript received July 4, 2017; revised November 24, 2017 and February 7, 2018; accepted March 18, 2018. Date of publication April 8, 2018; date of current version November 19, 2018. This work was supported in part by National Natural Science Foundation under Grant 51377065, Grant 61773284, and Grant 51707079, in part by Tianjin Young Elite Scientists Sponsorship Program under Grant TJSQNTJ201718, and in part by China Postdoctoral Science Foundation under Grant 2017M622443. Recommended for publication by Associate Editor B. G. Fernandes. *(Wei Xu and Yajie Jiang are co-first authors.) (Corresponding author: Chaoxu Mu.)*

W. Xu and Y. Jiang are with the State Key Laboratory of Advanced Electromagnetic Engineering and Technology, School of Electrical and Electronic Engineering, Huazhong University of Science and Technology, Wuhan 430074, China (e-mail:

φ_h	Initial angels of harmonics of back EMF.
ω_1	Angular frequency of the fundamental wave of back EMF.
ω_h	Angular frequencies of the harmonics of back EMF.
h	Order of the harmonics.
$\boldsymbol{E}_r(s)$	Laplace-transform of $\boldsymbol{e}_r$.
s	Laplace operator.
$\boldsymbol{\Psi}_{r\_I}(t) = [\psi_{r\alpha\_I}(t) \quad \psi_{r\beta\_I}(t)]^T$	Estimated rotor flux by pure integrator (α, β axes, respectively).
ω_c	Cut-off frequency of the LPF.
$\boldsymbol{\Psi}_{r\_\mathrm{LPF}}(t) = [\,\psi_{r\alpha\_\mathrm{LPF}}(t)\ \psi_{r\beta\_\mathrm{LPF}}(t)\,]^T$	Estimated rotor fluxes by LPF (α, β axes, respectively).
ω'	Center frequency of SOGI.
k	Coefficient of SOGI.
$\boldsymbol{\Psi}_{r\_\mathrm{SOIFO}}(s) = [\,\psi_{r\alpha\_\mathrm{SOIFO}}(s)\ \psi_{r\beta\_\mathrm{SOIFO}}(s)\,]^T$	Observed rotor fluxes by SOIFO (α, β axes, respectively).
$\hat{\boldsymbol{E}}_r(s)$	Filtered output of $\boldsymbol{E}_r(s)$.
$\boldsymbol{\varepsilon}_{E_r}$	Intermediate variable of SOIFO.
Γ	Coefficient of SOIFO.
K_1, K_2	Coefficients of second-order SOGI.
$\boldsymbol{\Psi}_{r\_\mathrm{SOSOIFO}}(s) = [\,\psi_{r\alpha\_\mathrm{SOSOIFO}}(s)\ \psi_{r\beta\_\mathrm{SOSOIFO}}(s)\,]^T$	Observed rotor fluxes by second-order SOIFO (α, β axes, respectively).
t_s	Setting time.
T_s	Sample period.

I. INTRODUCTION

PMSM drive system with the FOC has been widely used in industrial applications, for its high performance, low torque ripple, fast current response, etc. In general, the mechanical sensor can provide the necessary rotor position information for the implementation of FOC, which leads to higher cost and lower reliability of PMSM drive. Therefore, the rotor position estimation involving sensorless control technique for PMSM drives is in the ascendant [1]–[4].

The sensorless control methods include high-frequency signal injection, back-EMF estimator, and rotor flux observer. For low-speed operations, the high-frequency signal injection methods, including sinusoidal wave and square wave, have been widely used in PMSM systems [5]–[7].

For medium- and high-speed regions, the universal sensorless control scheme is the back-EMF estimator, where the rotor position is extracted from the fundamental wave of back EMF [8]–[11]. The back-EMF extraction-based sensorless control algorithms can be implemented by various methods, for example, extended Kalman filter [1], [8], sliding mode observer [9], Luenberger observer [10], artificial intelligence-based estimator [11], etc. These methods have been investigated in a large amount of literature. However, the back EMF cannot be precisely extracted with noises at low speed [9]. Therefore, the back-EMF estimation scheme is not qualified at low speed.

Apart from the back EMF, the PMSM rotor position information can also be acquired from the rotor flux via direct trigonometric relations [12]. Benefiting from that the magnitude of rotor flux remains constant in the transient state, the rotor flux estimation method has the potential to become a general sensorless control scheme for the PMSM drive systems. However, the traditional rotor flux observation methods, i.e., the pure integrator and LPF, cannot provide the accurate rotor flux.

On basis of the PMSM voltage and flux models, the pure integrator is a universal part in building a traditional rotor flux observer [13], [14]. However, the dc offset and harmonics of the estimated flux are generated by the parameter mismatches, unknown integral initial value, voltage and current detection errors and converter disturbances. Hence, the accuracy of estimated speed and rotor position is very low. Especially, the observed flux would be deviated from the real flux because of the saturation effect, which is mainly caused by the unknown integral initial value [15]. Therefore, some works focus on improving the pure integrator-based rotor flux observer. In [14] and [15], one initial flux condition estimator-based gradient algorithm is developed to estimate the unknown integral initial value, which is used for the rotor flux compensation. In [16] and [17], the stability is introduced to rotor flux observer with new coefficients designs. A disturbance observer is proposed in [18], in which the rotor flux is obtained from the stator flux integrator. In [19], the parameter identification is used in rotor flux observation. Although these approaches can improve the estimation accuracy of rotor flux, the effectiveness and practicability of these methods cannot be guaranteed yet.

The LPF is another one of flux estimation methods which can effectively reduce the dc offset and harmonics, but it also leads to the amplitude attenuation and phase shift [14]. Meanwhile, the LPF method requires the rotor phase compensation, which means that the machine speed information is needed.

By intensively analyzing the existing work, the rotor flux observation-based sensorless control strategy has not been adequately investigated. Thanks to the advanced filter capability and low computational cost, the SOGI has been commonly used for filter, quadrature signal generation, and phase extraction [20], [21]. By analyzing its transfer functions, the SOGI can be considered as a filter combined with an integrator. Moreover, the amplitude attenuation and phase shift can be avoided. Thereby, in [22], the SOGI is used for stator flux estimation in an induction machine drive system.

Till date, the SOGI has not been used for flux observation in the PMSM drive system. Therefore, on the basis of SOGI, a novel second-order generalized integral flux observer (SOIFO) is designed in this paper, to remove the aforementioned drawbacks of both the pure integrator and LPF methods. However, the theoretical analysis shows that the dc-eliminating ability of the SOIFO is not excellent. To solve this problem, an improved second-order SOIFO structure is proposed. With a fourth-order transform function, the second-order SOIFO has strong attenuation ability against the dc offset and harmonics. So, the above application limitations of rotor flux observation in parameter mismatches, external disturbances, and unknown integral initial value are removed, while the rotor flux, rotor position, and speed are estimated accurately. The proposed sensorless control scheme can be used in many industrial applications, such as the electric vehicle, servo system, and so on. Its advantages contain wide speed region, simple implementation, abilities to eliminate the dc offset and harmonics. Thereby, the extra parameter identification and disturbance attenuation structures are not needed. Specially, the proposed method can be used at 1–100% rated speed region, while most back-EMF estimation-based sensorless control strategy could not work effectively below 5% rated speed region. Furthermore, the detailed discretization implementation of the second-order SOGI is also proposed in this paper.

The structure of this paper is organized as follows. In Section II, the traditional PMSM rotor flux observers and their performance are studied. The SOIFO and its second-order version for the PMSM rotor flux observation are proposed and intensively investigated in Section III. In Section IV, comprehensive experimental results are presented. Finally, conclusions are drawn in Section V.

II. CONVENTIONAL PMSM ROTOR FLUX OBSERVERS

As stated in [8], the voltage and flux equations of PMSM in the stationary coordinate can be described as

$$\boldsymbol{u}_s = R_s \cdot \boldsymbol{i}_s + p\boldsymbol{\Psi}_s \tag{1}$$

$$\boldsymbol{\Psi}_s = L \cdot \boldsymbol{i}_s + \psi_f \cdot \begin{bmatrix} \cos(\theta_e) \\ \sin(\theta_e) \end{bmatrix} \tag{2}$$

where $\boldsymbol{u}_s$ is the stator voltage vector, $\boldsymbol{i}_s$ is the stator current vector, $\boldsymbol{\psi}_s$ is the stator flux vector, $\boldsymbol{u}_s = [\,u_\alpha \; u_\beta\,]^T$, $\boldsymbol{i}_s = [\,i_\alpha \; i_\beta\,]^T$, $\boldsymbol{\psi}_s = [\,\psi_{s\alpha} \; \psi_{s\beta}\,]^T$, L is the stator inductance, R_s is the stator resistance, p is the differential operator, θ_e is the rotor electrical position, ψ_f is the flux linkage, u_α and u_β are the α- and β-axis stator voltages, i_α and i_β are the stator currents, and $\psi_{s\alpha}$ and $\psi_{s\beta}$ are the stator flux. The rotor flux of PMSM can be given as

$$\boldsymbol{\Psi}_r = \boldsymbol{\Psi}_s - L \cdot \boldsymbol{i}_s = \psi_f \begin{bmatrix} \cos(\theta_e) \\ \sin(\theta_e) \end{bmatrix} \tag{3}$$

where $\boldsymbol{\Psi}_r$ is the rotor flux vector, $\boldsymbol{\Psi}_r = [\,\psi_{r\alpha} \; \psi_{r\beta}\,]^T$. It can be seen that the rotor position and speed can be extracted from the rotor flux, which are given as

$$\theta_e = \tan^{-1}(\psi_{r\beta}/\psi_{r\alpha}) \tag{4}$$

$$p\theta_e = \omega_e \tag{5}$$

where ω_e is the rotor electrical angular velocity. The PMSM sensorless control based on the rotor flux observation is shown in Fig. 1, where $\hat{\boldsymbol{\Psi}}_r$ is the observed rotor flux vector, $\hat{\boldsymbol{\Psi}}_r = [\,\hat{\psi}_{r\alpha} \; \hat{\psi}_{r\beta}\,]^T$, $\hat{\theta}_e$ is the estimated rotor position, and $\hat{\omega}_e$ is the estimated speed.

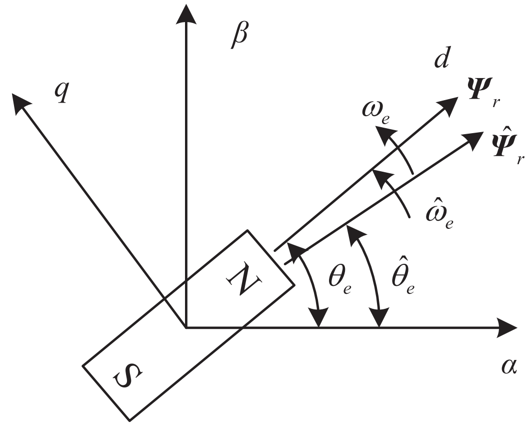

Fig. 1. PMSM sensorless control based on the rotor flux observation.

As shown in (1) and (4), rotor flux is the integration of back EMF, which can be given as

$$\boldsymbol{\Psi}_r = \int (\boldsymbol{u}_s - R_s\boldsymbol{i}_s - L \cdot p\boldsymbol{i}_s)\,dt = \int \boldsymbol{e}_r\,dt \tag{6}$$

where $\boldsymbol{e}_r$ is the back-EMF vector, $\boldsymbol{e}_r = [\,e_{r\alpha} \; e_{r\beta}\,]^T$. The integral initial value of the estimated rotor flux is defined as $\boldsymbol{\Psi}_r(0) = \boldsymbol{\Psi}_s(0) - L \cdot \boldsymbol{i}_s(0)$. Meanwhile, considering the disturbances of a practical PMSM drive system, i.e., parameter mismatches, unknown integral initial value, detection errors, and converter nonlinearities, (6) is modified as

$$\begin{aligned}\boldsymbol{\Psi}_r = \int \big(&\boldsymbol{u}_s - (R_{s0} + \Delta R_s))\,\boldsymbol{i}_s - (L_0 + \Delta L) \cdot p\boldsymbol{i}_s \\ &+ \boldsymbol{e}_{r0} + \boldsymbol{\chi}\big)dt\end{aligned} \tag{7}$$

where R_{s0} and L_0 are the fixed nominal parameters, ΔR_s and ΔL are the parameter variations, $\boldsymbol{e}_{r0}$ is the initial back-EMF vector, $\boldsymbol{e}_{r0} = [\,e_{r\alpha 0} \; e_{r\beta 0}\,]^T$, $\int \boldsymbol{e}_{r0}\,dt = \boldsymbol{\Psi}_r(0)$, and $\boldsymbol{\chi}$ represents the other disturbances. Then, the back EMF can be written as

$$\boldsymbol{e}_r = \boldsymbol{A}_o + \boldsymbol{A}_1 \sin(\omega_1 t + \varphi_1) + \sum \boldsymbol{A}_h \sin(\omega_h t + \varphi_h) \tag{8}$$

where $\boldsymbol{A}_0$ is the dc component, $\boldsymbol{A}_0 = [A_{0\alpha} \quad A_{0\beta}]^T$, $\boldsymbol{A}_1 \sin(\omega_1 t + \varphi_1)$ is the fundamental component, $\boldsymbol{A}_1$ is the amplitude of fundamental wave, $\boldsymbol{A}_1 = [\,A_{1\alpha} \; A_{1\beta}\,]^T$, $\sum \boldsymbol{A}_h \sin(\omega_h t + \varphi_h)$ is the sum of harmonics, $\boldsymbol{A}_h$ is the amplitude of harmonics, $\boldsymbol{A}_h = [\,A_{h\alpha} \; A_{h\beta}\,]^T$, φ_1 and φ_h are the initial angels of fundamental wave and harmonics of the back EMF, ω_1 and ω_h are the corresponding angular frequencies, and h is the order of harmonics. Take Laplace transformation of (8), it can be written as

$$\begin{aligned}\boldsymbol{E}_r(s) = \frac{\boldsymbol{A}_o}{s} + \boldsymbol{A}_1 \frac{s\sin\varphi_1 + \omega_1\cos\varphi_1}{s^2 + \omega_1^2} \\ + \sum \boldsymbol{A}_h \frac{s\sin\varphi_h + \omega_h\cos\varphi_h}{s^2 + \omega_h^2}\end{aligned} \tag{9}$$

where $\boldsymbol{E}_r(s)$ is the Laplace transform of $\boldsymbol{e}_r$, and s the Laplace operator. Taking pure integrator 1/s as flux observer, the observed rotor flux $\boldsymbol{E}_r(s)\cdot 1/s$ can be given as

$$\boldsymbol{\Psi}_{r\_I}(t) = \boldsymbol{A}_o t + \frac{\boldsymbol{A}_1}{\omega_1}\sin(\omega_1 t+\varphi_1-0.5\pi) + \boldsymbol{A}_1\frac{\cos(\varphi_1)}{\omega_1} + \sum\frac{\boldsymbol{A}_h}{\omega_h}\sin(\omega_h t+\varphi_h-0.5\pi)+\sum\boldsymbol{A}_h\frac{\cos(\varphi_h)}{\omega_h} \qquad (10)$$

where $\boldsymbol{\Psi}_{r\_I}(t)$ is the estimated rotor flux vector by the pure integrator, $\boldsymbol{\Psi}_{r\_I}(t) = [\,\psi_{r\alpha\_I}(t)\ \psi_{r\beta\_I}(t)\,]^T$. In (10), except the fundamental part $\boldsymbol{A}_1\cdot\sin(\omega_1 t+\varphi_1-0.5\pi)/\omega_1$, the dc component and harmonics are also contained in the estimated rotor flux. Moreover, the dc component consists of two parts, where $\boldsymbol{A}_1\frac{\cos(\varphi_1)}{\omega_1}+\sum\boldsymbol{A}_h\frac{\cos(\varphi_h)}{\omega_h}$ is constant, and $\boldsymbol{A}_o t$ linearly increases with time. Especially, the time-increasing term $\boldsymbol{A}_o t$, resulted from the integral initial value, would lead to the saturation and serious distortion of flux. In this case, the sensorless control cannot be achieved ultimately. In addition, the harmonics of estimated rotor flux also affect the accuracy of position observation, especially when the PMSM is operated at low speed.

Another rotor flux estimator is LPF: $1/(s+\omega_c)$, where ω_c is the cut-off frequency. Taking the inverse Laplace transform of $\boldsymbol{E}_r(s)\cdot 1/(s+\omega_c)$, the estimated rotor flux can be described as

$$\begin{aligned}\boldsymbol{\Psi}_{r\_\mathrm{LPF}}(t) &= \frac{\boldsymbol{A}_o}{\omega_c} - \frac{\boldsymbol{A}_o}{\omega_c}e^{-\omega_c t} + \frac{\boldsymbol{A}_1}{\sqrt{\omega_1^2+\omega_c^2}}\\ &\quad\times\sin(\omega_1 t+\varphi_1-0.5\pi+\theta_1)\\ &\quad+\boldsymbol{A}_1\frac{\cos(\varphi_1+\theta_1)}{\sqrt{\omega_1^2+\omega_c^2}}e^{-\omega_c t}+\sum\frac{\boldsymbol{A}_h}{\sqrt{\omega_h^2+\omega_c^2}}\\ &\quad\times\sin(\omega_h t+\varphi_h-0.5\pi+\theta_h)\\ &\quad+\sum\boldsymbol{A}_h\frac{\cos(\varphi_h+\theta_h)}{\sqrt{\omega_h^2+\omega_c^2}}\end{aligned} \qquad (11)$$

where $\boldsymbol{\Psi}_{r\_\mathrm{LPF}}(t)$ is the estimated rotor flux vector by LPF, $\boldsymbol{\Psi}_{r\_\mathrm{LPF}}(t) = [\,\psi_{r\alpha\_\mathrm{LPF}}(t)\ \psi_{r\beta\_\mathrm{LPF}}(t)\,]^T$. From (11), it can be seen that the main dc offset would exponentially decay as time goes by. Although the sight dc component, $\sum\boldsymbol{A}_h\frac{\cos(\varphi_h+\theta_h)}{\sqrt{\omega_h^2+\omega_c^2}}$ exists, the influence of saturation-effect has been removed. Meanwhile, the amplitudes of harmonics are reduced. However, the phase shifts, $\theta_1 = \arctan(\omega_c/\omega_1)$, $\theta_h = \arctan(\omega_c/\omega_h)$, and the amplitude attenuations $\boldsymbol{A}_1/\sqrt{\omega_1^2+\omega_c^2}$, $\boldsymbol{A}_h/\sqrt{\omega_1^2+\omega_c^2}$, are generated by LPF. Therefore, the LPF-based rotor position estimation relies on the phase compensation rigidly.

III. FLUX OBSERVER-BASED SECOND-ORDER SOIFO

To eliminate the limitations of the traditional methods, a SOIFO on basis of the SOGI structure is first proposed for the PMSM rotor flux observation in this paper. With the SOIFO, the dc offset and harmonics in the observed rotor flux are reduced. Furthermore, an improved second-order SOIFO with a four-order transform function is designed to enhance the ability to eliminate the dc offset and harmonics.

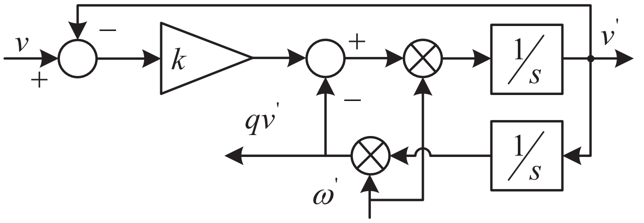

Fig. 2. Structure of SOGI.

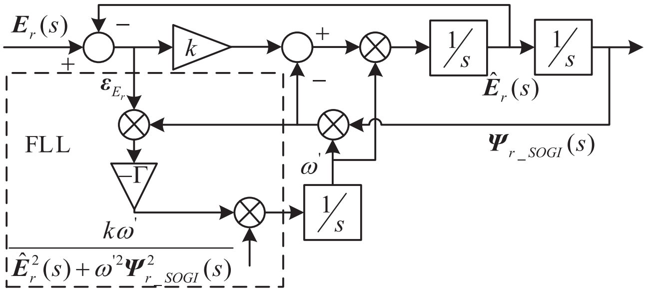

Fig. 3. Diagram of SOIFO.

A. SOIFO

As stated in [23], the SOGI has been used for the phase and amplitude extractions of grid voltage. Its structure is shown in Fig. 2.

In Fig. 2, v is the input signal; v' and qv' are two outputs. The transfer functions are given as

$$D(s) = \frac{v'(s)}{v(s)} = \frac{k\omega' s}{s^2+k\omega' s+\omega'^2} \qquad (12)$$

$$Q(s) = \frac{qv'(s)}{v(s)} = \frac{k\omega'^2}{s^2+k\omega' s+\omega'^2} \qquad (13)$$

where ω' is the center frequency. It is well known that $D(s)$ is used for filtering, and $Q(s)$ is used for the integration. In the steady state, it is defined $s = j\omega'$. Then, qv' can be seen as the integration of the input, calculated by

$$Q(s) = \frac{k\omega'^2}{k\omega' s+\omega'^2-\omega'^2} = \frac{k\omega'^2}{-\omega'^2+k\omega' s+\omega'^2} = \frac{\omega'}{s}. \qquad (14)$$

As shown in (14), $Q(s)$ can be considered as an integrator. In this way, a novel PMSM rotor flux observation method, SOIFO, can be constructed as

$$\begin{aligned}\boldsymbol{\Psi}_{r\_\mathrm{SOIFO}}(s) &= \frac{1}{\omega'}\cdot Q(s)\cdot\boldsymbol{E}_r(s)\\ &= \frac{k\omega'}{s^2+k\omega' s+\omega'^2}\cdot\boldsymbol{E}_r(s) = \frac{1}{s}\cdot\boldsymbol{E}_r(s)\end{aligned} \qquad (15)$$

where $\boldsymbol{\Psi}_{r\_\mathrm{SOIFO}}(s)$ is the observed rotor flux vector by SOIFO, $\boldsymbol{\Psi}_{r\_\mathrm{SOIFO}}(s) = [\,\psi_{r\alpha\_\mathrm{SOIFO}}(s)\ \psi_{r\beta\_\mathrm{SOIFO}}(s)\,]^T$. The structure of SOIFO is shown in Fig. 3. In order to guarantee $\omega' = \omega_1$, a frequency-locked loop (FLL) is also proposed with SOIFO. In the figure, $\hat{\boldsymbol{E}}_r(s)$ is the filtered output, $\boldsymbol{\varepsilon}_{E_r}$ is an intermediate variable, and Γ is a coefficient.

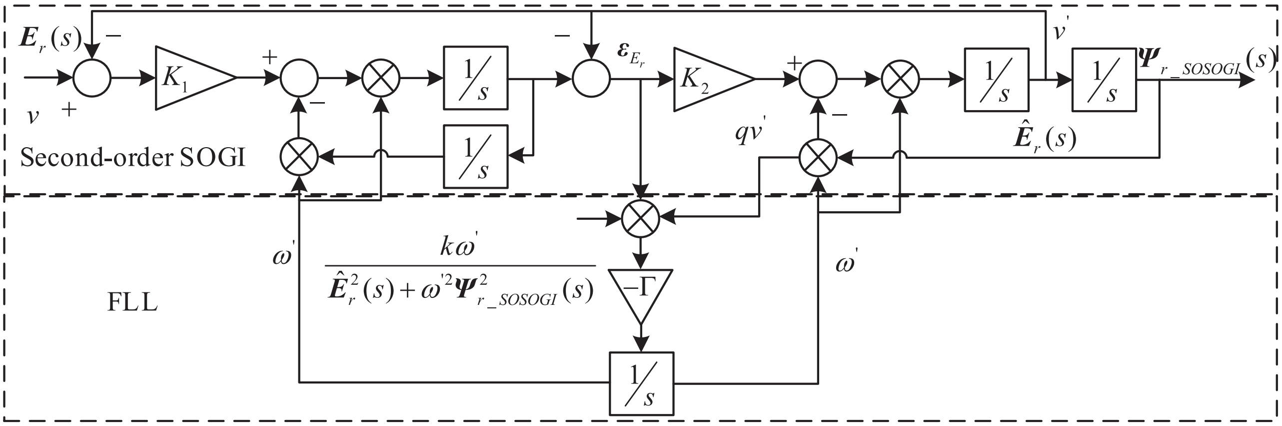

Fig. 4. Diagram of second-order SOIFO/SOGI.

Combining with (9), the estimated rotor flux is given as

$$\begin{aligned}\boldsymbol{\Psi}_{r\_\mathrm{SOIFO}}(t) &= \frac{\boldsymbol{A}_o k}{\omega_1} + \frac{\boldsymbol{A}_1}{\omega_1}\sin(\omega_1 t + \varphi_1 - 0.5\pi)\\ &\quad + \sum \frac{1}{\sqrt{(1-h^2)^2/k^2h^2+1}} \cdot \frac{\boldsymbol{A}_h}{\omega_h}\\ &\quad \times \sin(\omega_h t + \varphi_h - 0.5\pi + \gamma_{h1}) \end{aligned}\tag{16}$$

where $\gamma_{h1} = \tan^{-1}(\frac{\omega'^2-\omega_h^2}{k\omega'\omega_h})$ and $h = \omega_h/\omega'$. The detailed calculation is provided in Appendix C. As shown in (16), with the reduced dc offset of estimated rotor flux, the saturation effect is removed without both phase shift and amplitude attenuation. Meanwhile, the magnitude of harmonics is inversely proportional to $\sqrt{(1-h^2)^2/k^2h^2+1}$, which can be simplified as $\sqrt{(1-h^2)^2/k^2h^2+1} \approx h/k \gg 1$. It means that the amplitudes of harmonics are reduced. The dc component of rotor flux is reduced to $\boldsymbol{A}_o k/\omega_1$. However, because $\boldsymbol{\Psi}_{r\_\mathrm{SOIFO}}(t)$ is the low-pass-filtered version of the input, the dc component of rotor flux by SOIFO cannot be removed completely, which would result in a rotor position estimation error.

B. Second-Order SOIFO

Recently, a novel second-order SOGI with enhanced ability to reject harmonic and dc offset is introduced in [21]. The transform functions of second-order SOGI are described as

$$\begin{aligned}D_1(s) &= \frac{v'(s)}{v(s)}\\ &= \frac{K_1K_2\omega'^2s^2}{s^4 + K_2\omega's^3 + (2+K_1K_2)\omega'^2s^2 + K_2\omega'^3s + \omega'^4}\end{aligned}\tag{17}$$

$$\begin{aligned}Q_1(s) &= \frac{qv'(s)}{v(s)}\\ &= \frac{K_1K_2\omega'^3s}{s^4 + K_2\omega's^3 + (2+K_1K_2)\omega'^2s^2 + K_2\omega'^3s + \omega'^4}\end{aligned}\tag{18}$$

where K_1 and K_2 are two coefficients. Similarly with SOGI, $D_1(s)$ is used for filtering, and $Q_1(s)$ is used for the integration. In the steady state, it is defined $s = j\omega'$, then qv' can be regarded as the integration of *v*. The relationship between the input and $qv'(s)$ of second-order SOGI can be equally accessed as

$$\begin{aligned}Q_1(s) &= \frac{K_1K_2\omega'^3s}{\omega'^4 - jK_2\omega'^4 + K_1K_2\omega'^2s^2 - 2\omega'^4 + jK_2\omega'^4 + \omega'^4}\\ &= \omega'\frac{1}{s}.\end{aligned}\tag{19}$$

Taking the back EMF as the input of second-order SOGI, qv' can be considered as the integration of back EMF. By further modification, the second-order SOIFO can be obtained as

$$\begin{aligned}\boldsymbol{\Psi}_{r\_\mathrm{SOSOIFO}}(s) &= \frac{1}{\omega'}\\ &\quad \times \frac{K_1K_2\omega'^3s}{s^4 + K_2\omega's^3 + (2+K_1K_2)\omega'^2s^2 + K_2\omega'^3s + \omega'^4}\\ &\quad \cdot \boldsymbol{E}_r(s) = \frac{1}{s}\cdot\boldsymbol{E}_r(s)\end{aligned}\tag{20}$$

where $\boldsymbol{\Psi}_{r\_\mathrm{SOSOIFO}}(s)$ is the observed rotor flux vector by second-order SOIFO, $\boldsymbol{\Psi}_{r\_\mathrm{SOSOIFO}}(s) = [\psi_{r\alpha\_\mathrm{SOSOIFO}}(s)\ \psi_{r\beta\_\mathrm{SOSOIFO}}(s)]^T$. The structure of second-order SOIFO is given in Fig. 4, where an FLL is applied for the frequency adaption. And the steady-state time domain of (20) is written as

$$\begin{aligned}\boldsymbol{\Psi}_{r\_\mathrm{SOSOIFO}}(t) &= \frac{\boldsymbol{A}_1}{\omega_1}\sin(\omega_1 t + \varphi_1 - 0.5\pi)\\ &\quad + \sum \frac{1}{\sqrt{\frac{[1-h^2(2+K_1K_2)+h^4]^2}{(h^2K_1K_2)^2} + \frac{(hK_2-h^3K_2)^2}{(h^2K_1K_2)^2}}}\\ &\quad \cdot \frac{\boldsymbol{A}_h}{\omega_h}\sin(\omega_h t + \varphi_h - 0.5\pi + \gamma_{h2})\end{aligned}\tag{21}$$

where $\gamma_{h2} = \tan^{-1}(\frac{K_2\omega'\omega_h^3 - K_2\omega'^3\omega_h}{\omega'^4 - h^2(2+K_1K_2)\omega'^2\omega_h^2 + \omega_h^4})$. The detailed calculation process has been proposed in Appendix D. Equation (21) shows that the dc component of the rotor flux observation is eliminated. Meanwhile, the magnitude

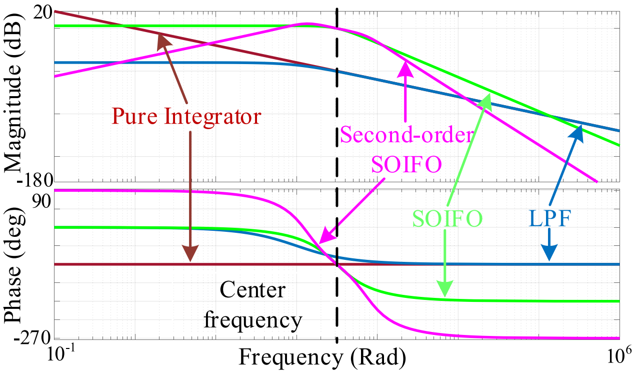

Fig. 5. Bode diagram of pure integrator, LPF, SOIFO, and second-order SOIFO.

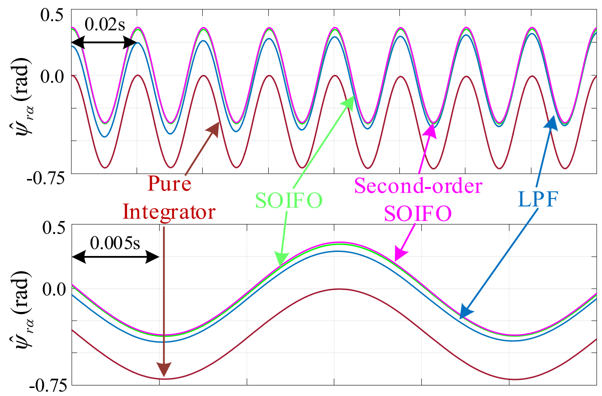

Fig. 6. Simulation results of α-axis rotor flux observation.

TABLE I
SUMMARIZATION OF KEY PERFORMANCE INDEXES

Observers	**dc offset**	**Harmonics**	**Saturation**	**Amplitude attenuation**	**Phase shift**
Pure integrator	Large	High	✓	×	×
LPF	None	Low	×	✓	✓
SOIFO	Low	Low	×	×	×
Second-order SOIFO	None	Lower	×	×	×

of high-order harmonics is inversely proportional to $\sqrt{\frac{[1-h^2(2+K_1K_2)+h^4]^2}{(h^2K_1K_2)^2}+\frac{(hK_2-h^3K_2)^2}{(h^2K_1K_2)^2}}$, which can be simplified as $\sqrt{\frac{[1-h^2(2+K_1K_2)+h^4]^2}{(h^2K_1K_2)^2}+\frac{(hK_2-h^3K_2)^2}{(h^2K_1K_2)^2}} \approx \frac{h^2}{K_1K_2} \gg \frac{h}{k} \gg 1$. It means that the second-order SOIFO can produce the lower gain magnitude at higher frequencies than that of SOIFO. The transfer functions and observed rotor flux of the four methods are summarized in Appendixes A and B, respectively.

The comparison of the four methods is further illustrated by the Bode diagram in Fig. 5, where the center frequency is $\omega' = \omega_1 = 100\,\pi$ rad/s, and the cut-off frequency of LPF is $\omega_c = 100$ rad/s. Meanwhile, the coefficients, k, K_1, and K_2 are described as 1.414, 1.56, and 3.11 respectively, where the setting time t_s of SOIFO and second-order SOIFO are both kept as 0.018 s.

From the previous analysis and Bode diagram, the proposed flux observation methods can be concluded as follows.

1) Due to the pole of pure integrator at the origin, the dc gain is infinite. The ideally dc inputs will result in a ramp output, which leads to some saturation. It has poor ability to attenuate the harmonics.
2) The LPF provides the attenuation of dc component, and its magnitude frequency response decays at a rate of –20 dB/decade at high frequency. However, the phase shift and the amplitude attenuation of fundamental wave are generated by it.
3) The SOIFO can obtain better magnitude attenuation of harmonics, reaching –40 dB/decade beyond center frequencies. However, its attenuation of lower frequency is 0 dB/decade, which means that it is sensitive to the dc offset.
4) The ideal dc component and harmonics attenuation capability are demonstrated by the second-order SOIFO, whose magnitude frequency response decays at rates of -20 and -60 dB/decade at lower and higher frequencies, respectively. With the negative magnitude response in the low-frequency and dc regions, the second-order SOIFO can eliminate dc component very well.

Using the similar coefficients of Fig. 5, the simulations of the proposed rotor flux observation methods are given in Fig. 6. In this figure, it can be seen that large dc offset exists in the estimated flux by pure integrator. The amplitude attenuation and the phase shift are generated by LPF. Although the estimated flux of SOIFO is similar to the second-order SOIFO, it can just limit dc component to a certain value. This has been proved by experimental results in Section IV. Some key performance indexes of the four methods can be summarized in Table I.

In [20], one discretization method is provided for the SOGI. Then, it has been widely used in many papers and engineering applications. Thereby, the discrete implementation of the second-order SOGI/SOIFO is given in this section. In order to acquire the ideal performance, the trapezoidal method is used as $s = \frac{2}{T_s}\frac{z-1}{z+1} = f_z$. In this way, the discrete forms of (17) and (18) can be written as

$$D_1(z) = \frac{K_1K_2\omega'^2 f_z^2}{f_z^4 + K_2\omega' f_z^3 + (2+K_1K_2)\omega'^2 f_z^2 + K_2\omega'^3 f_z + \omega'^4} \tag{22}$$

$$Q_1(z) = \frac{K_1K_2\omega'^3 f_z}{f_z^4 + K_2\omega' f_z^3 + (2+K_1K_2)\omega'^2 f_z^2 + K_2\omega'^3 f_z + \omega'^4}. \tag{23}$$

It defines $u = 2K_1K_2\omega'^2T_s^2$, $v = 8K_2\omega'T_s$, $w = 4(2+K_1K_2)\omega'^2T_s^2$, $x = 2K_2\omega'^3T_s^3$, and $y = \omega'^4T_s^4$. Substituting $b_0 = \frac{u}{16+v+w+x+y}$, $a_1 = \frac{-64-2v+2x+4y}{16+v+w+x+y}$, $a_2 = \frac{96-2w+6y}{16+v+w+x+y}$, $a_3 = \frac{-64+2v-2x+4y}{16+v+w+x+y}$, and $a_4 = \frac{16-v+w-x+y}{16+v+w+x+y}$ into (22) and (23), and the final discretized forms of $Q_1(s)$ and $D_1(s)$ are given as

$$Q_1(z) = \frac{b_0\omega'T_s\left(1+2z^{-1}-2z^{-3}-z^{-4}\right)}{1+a_1z^{-1}+a_2z^{-2}+a_3z^{-3}+a_4z^{-4}} \tag{24}$$

$$D_1(z) = \frac{2b_0\left(1-2z^{-2}+z^{-4}\right)}{1+a_1z^{-1}+a_2z^{-2}+a_3z^{-3}+a_4z^{-4}}. \tag{25}$$

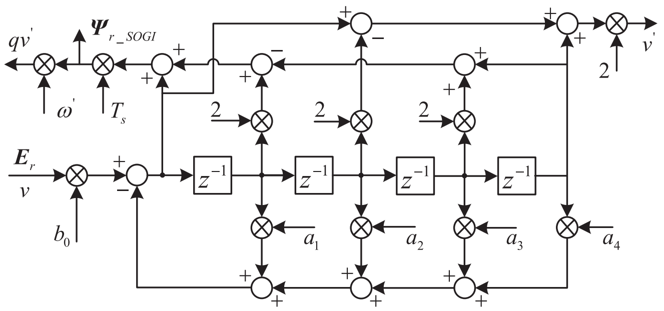

Fig. 7. Trapezoidal discrete implementation of the second-order SOIFO or SOGI.

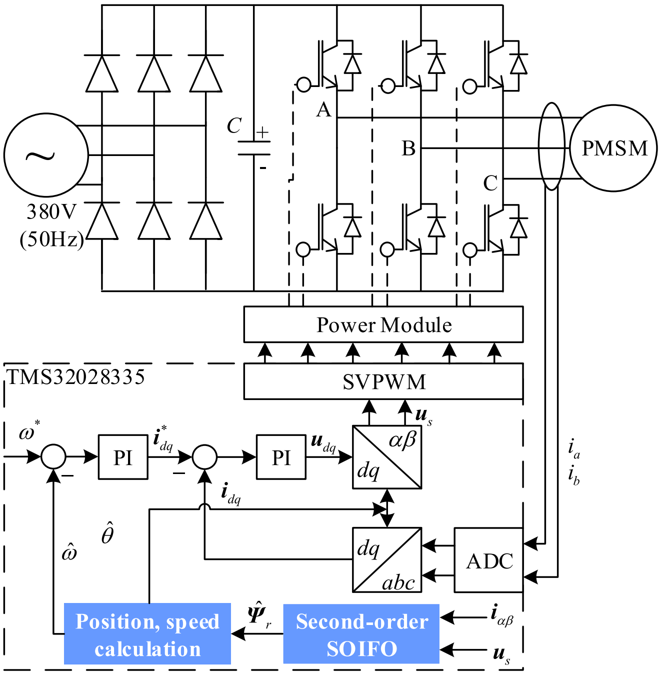

Fig. 8. Block diagram of the experimental bench.

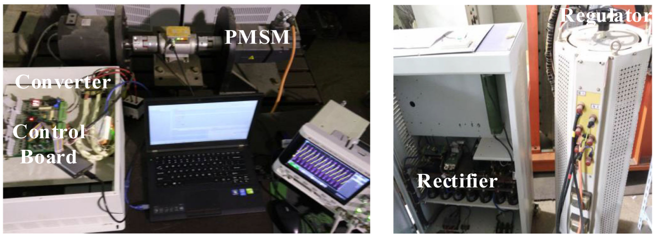

(a) (b)

Fig. 9. PMSM experimental platform.

The trapezoidal discrete implementation structure of the second-order SOIFO or SOGI is shown in Fig. 7.

IV. EXPERIMENTAL RESULTS

The proposed sensorless control strategy is implemented in a TI TMS320F28335 DSP board, and the block diagram of drive

TABLE II
MAIN PARAMETERS OF THE PMSM

Symbols	Parameters	Values
Φ_f	Flux linkage of permanent magnet	0.35 Wb
n_N	Rated speed	2000 rpm
n_p	Pole-pair number	3
L	d- and q- axis inductance	5.0 mH
R_s	Stator resistance	0.8 Ω
T_N	Rated torque	14 N · m
J	Rotational inertia	$3.78*10^{-4}$ kg · m^2

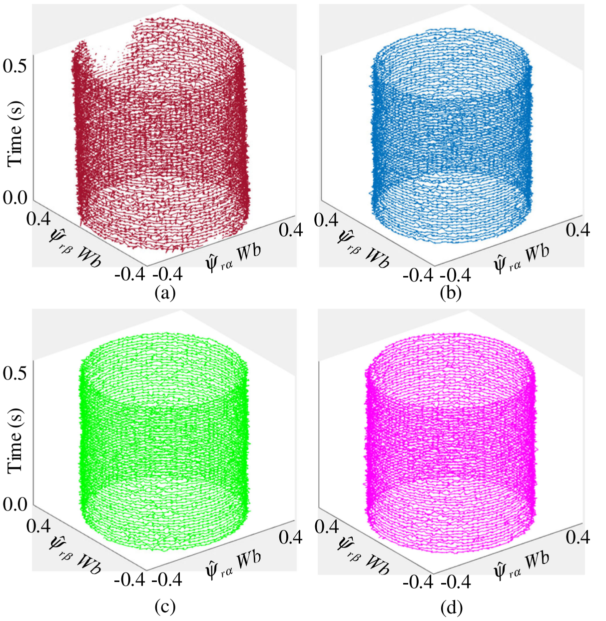

(a) (b) (c) (d)

Fig. 10. Three-dimensional rotor flux trajectories. (a) Pure integrator. (b) LPF. (c) SOIFO. (d) Second-order SOIFO.

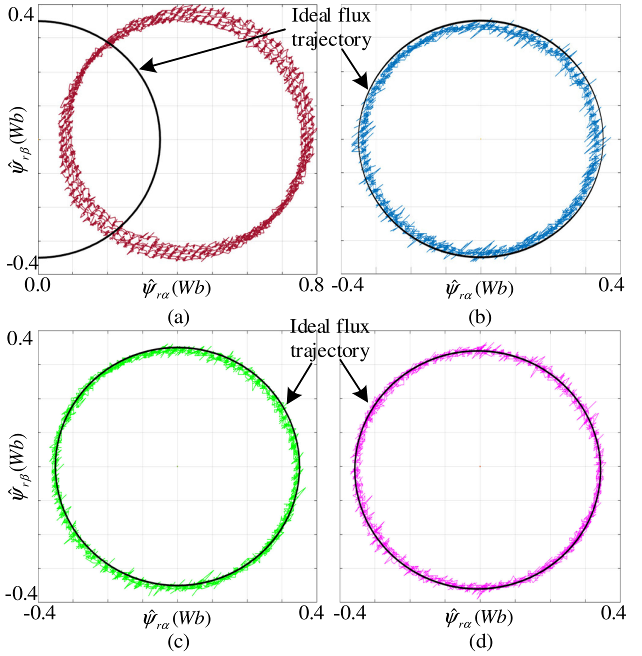

(a) (b) (c) (d)

Fig. 11. Rotor flux circles. (a) Pure integrator. (b) LPF. (c) SOIFO. (d) Second-order SOIFO.

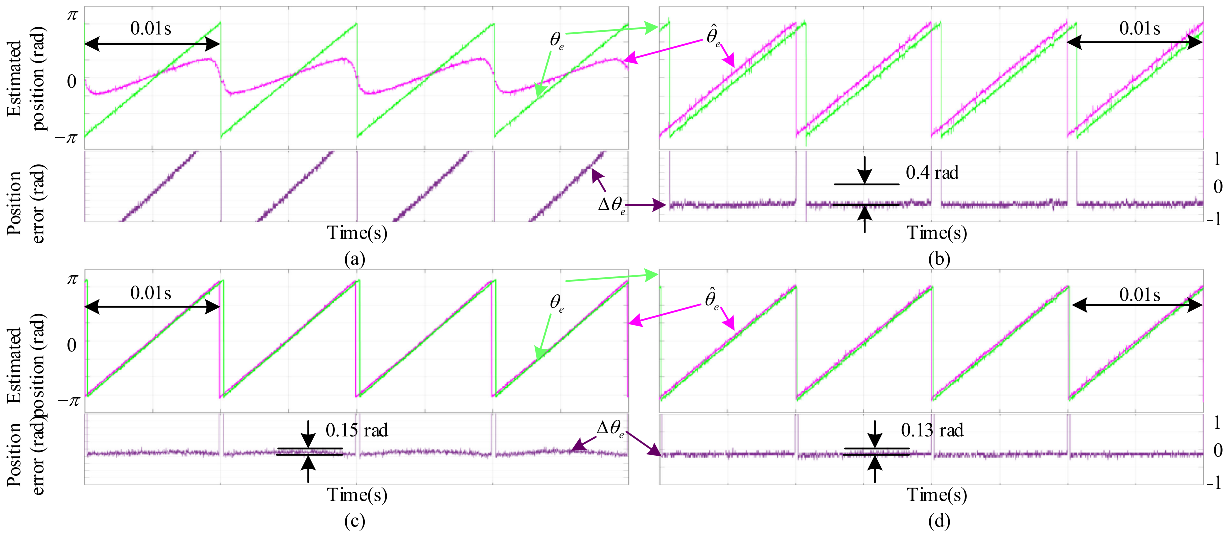

Fig. 12. Rotor position estimation at 2000 r/min. (a) Pure integrator. (b) LPF. (c) SOIFO. (d) Second-order SOIFO.

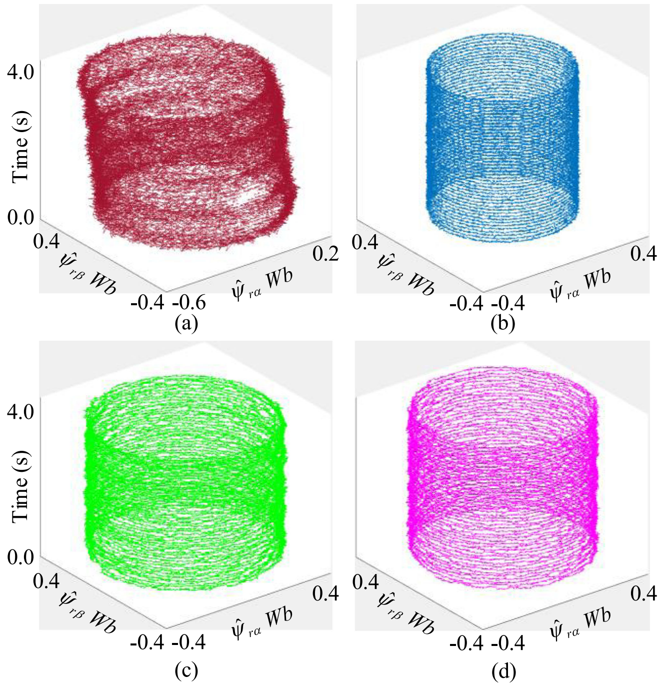

Fig. 13. Three-dimensional rotor flux trajectories. (a) Pure integrator. (b) LPF. (c) SOIFO. (d) Second-order SOIFO.

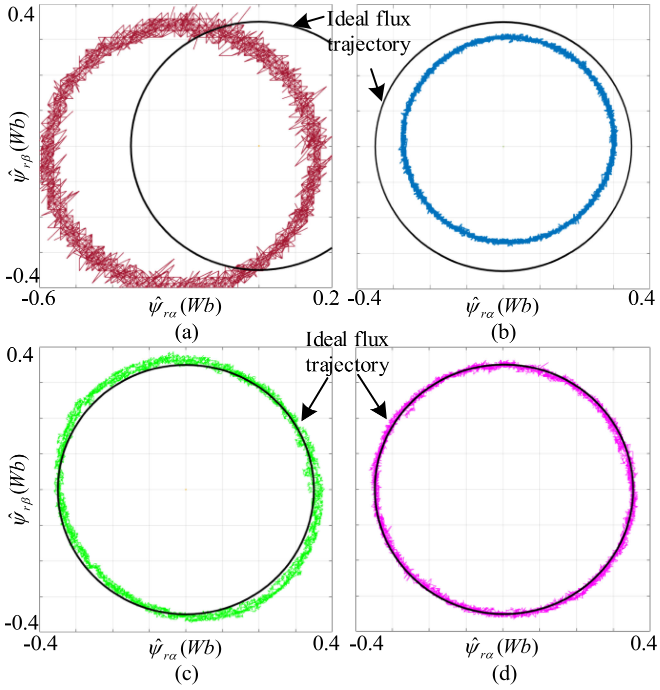

Fig. 14. Rotor flux circles. (a) Pure integrator. (b) LPF. (c) SOIFO. (d) Second-order SOIFO.

system is shown in Fig. 8. In the system, a three-phase uncontrolled rectifier is used for providing the dc power, where the three-phase pulsewidth modulation converter conducts alternative current for the PMSM drive. The control frequency of speed loop is 1 kHz, and the sampling frequency of current loop and sensorless control algorithm is 10 kHz. Main drive indexes are outputted to a digital oscilloscope through the D/A converter modules on the DSP board. As shown in the picture, the FOC is used as the basic control scheme. The rotor flux is estimated by the proposed pure integrator, LPF, SOIFO, and second-order SOIFO, respectively. Since the $s = j\omega'$ is contained in the denominator of (13) and (18), the SOIFO or second-order SOIFO cannot operate at zero speed or be used for start-up. In this paper, the PMSM uses open-loop start-up, and later switches to sensorless operation. The PMSM experimental platform is shown in Fig. 9. Main parameters of the PMSM are listed in Table II.

To achieve the same setting time of SOIFO and second-order SOIFO, the experiential coefficients k, K_1, and K_2 are taken as 1.414, 1.56, and 3.11, respectively.

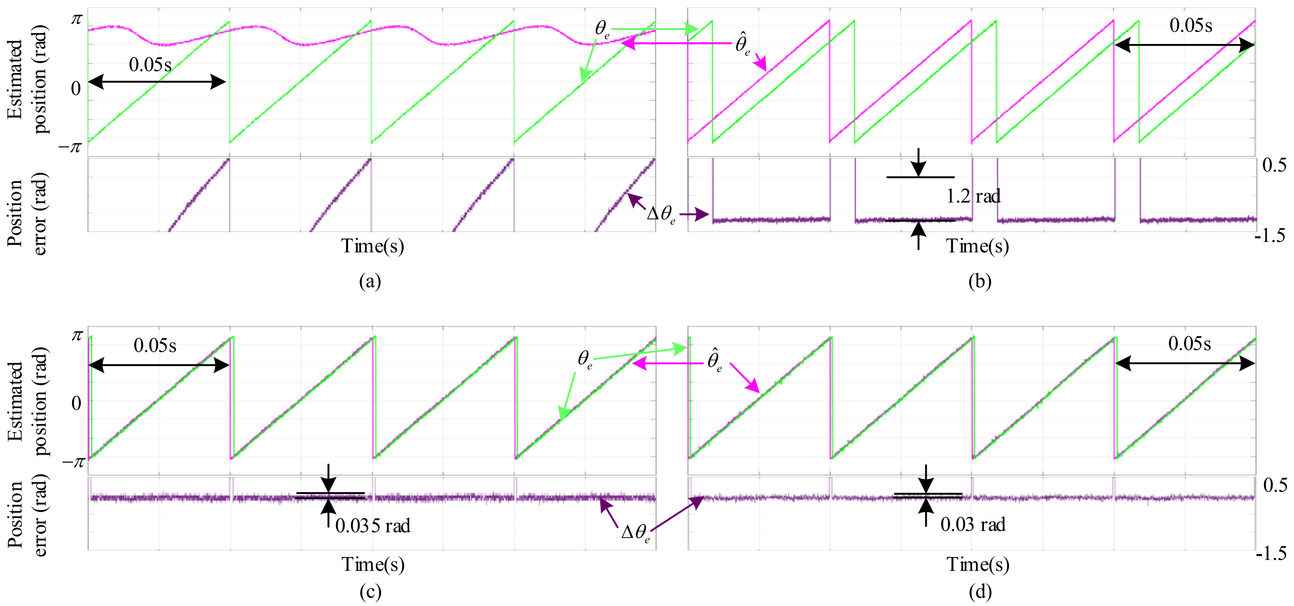

(a) (b) (c) (d)

Fig. 15. Rotor position estimation at 400 r/min. (a) Pure integrator. (b) LPF. (c) SOIFO. (d) Second-order SOIFO.

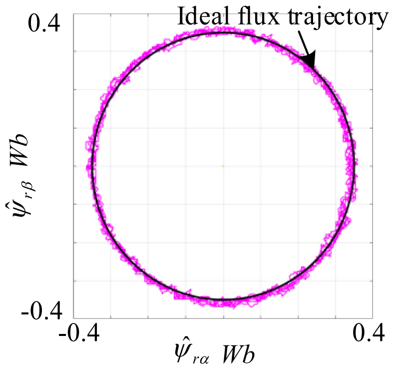

Fig. 16. Rotor flux trajectory at 20 r/min by second-order SOIFO.

A. Steady-State Performance

The estimated rotor flux trajectories with the four methods at a high speed (2000 r/min, 0 N·m) are shown in Figs. 10 and 11, respectively. As can be seen, the estimated rotor flux of pure integrator is deviated from the actual flux circle. Its deviation quantity increases with time, which results in some saturation in the rotor flux. The amplitude attenuation is generated by LPF. Meanwhile, the estimated rotor flux of SOIFO and second-order SOIFO are consistent with the actual rotor flux. The performance can be further illustrated by the overhead rotor flux cycles in Fig. 11, in which the black curves stand for the actual flux cycles. Compared with the flux deviation of pure integrator and the amplitude attenuation of LPF, the proposed methods can provide precise flux observation without drawbacks. Then, the estimated rotor positions are shown in Fig. 12. It should be noted that the phase shift is generated by LPF, which is shown in the rotor position estimation error, 0.4 rad. Especially, the rotor position estimation errors by SOIFO and second-order SOIFO are 0.15 and 0.13 rad, respectively. As shown in the figure, the flux and position estimation by second-order SOIFO are more accurate than those of SOIFO.

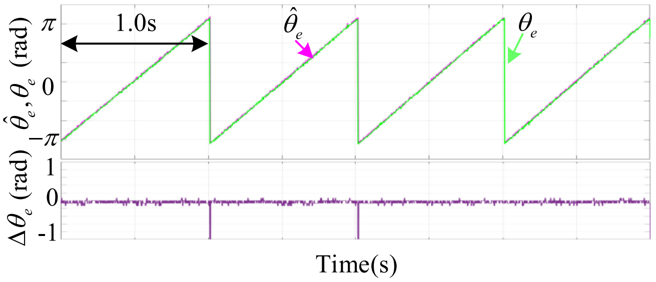

Fig. 17. Position estimation at 20 r/min by second-order SOIFO.

Figs. 13 and 14 show the estimated rotor flux trajectories at a medium speed (400 r/min, 0 N·m). The results are similar with those of high speed, i.e., vertically eccentric rotor flux of pure integrator, amplitude attenuation of LPF. As the distortion appears in the estimated rotor flux by the SOIFO method, the best flux estimation result is produced by the second-order SOIFO. The estimated rotor positions and their errors are given in Fig. 15. In these figures, the position estimation errors of pure integrator, LPF, SOIFO, and second-order SOIFO are 6.0, 1.2, 0.035, and 0.03 rad, respectively. It should be noted that the phase shift and amplitude attenuation of LPF are more severe at relatively low speed.

Except the performance analysis at mid- and high-speed regions, the accurate rotor flux and the position estimation of second-order SOIFO at the 1.0% rated speed (20 r/min) region are also given in Figs. 16 and 17 separately. To avoid redundancy, the results of other methods are not presented. As shown in Figs. 11–17, it can be concluded that the limitations of conventional sensorless control methods for rotor flux observation

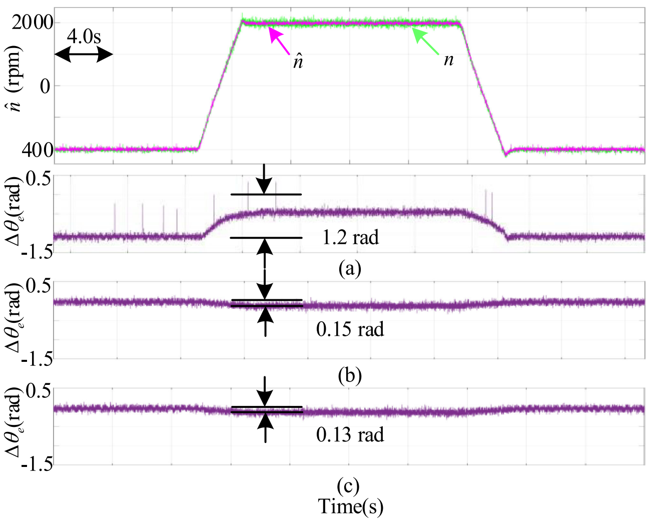

Fig. 18. Experimental comparison of speed and position estimation errors during continuous speed variation without load. (a) LPF. (b) SOIFO. (c) Second-order SOIFO.

are solved by the proposed SOIFO and second-order SOIFO, and the latter is better.

B. Dynamic Performance

To further verify the proposed observer, the estimations of speed variation between 400 and 2000 r/min of LPF, SOIFO, and second-order SOIFO are presented in Fig. 18. It should be noted that the speed can be well estimated by the three methods. However, the rotor position estimation errors vary widely, which are 1.2 rad of LPF, 0.15 rad of SOIFO, and 0.13 rad of second-order SOIFO. Especially, the rotor position estimation error of second-order SOIFO is caused by the sampling period delay, which could occupy a large proportion in a motor rotating period at high speed. Therefore, the rotor position estimation error caused by the delay is relatively large, and vice versa.

Fig. 19 shows the dynamic performance of the three methods during a step load disturbance from 0 to 10 N·m at 2000 r/min. In the figures, the rotor position estimation errors of LPF, SOIFO, and second-order SOIFO are 1.3, 0.25, and 0.20 rad, respectively. As can be seen, the oscillation of estimation error for rotor position is appeared with LPF. The phenomenon is eliminated by SOIFO and second-order SOIFO. As shown in Figs. 18 and 19, the SOIFO and second-order SOIFO can provide accurate rotor position during the dynamic process.

As mentioned above, since $s = j\omega'$ is contained in the denominator of SOIFO and second-order SOIFO, it cannot operate at zero speed or be used for start-up. Thereby, the open-loop startup is adopted in this paper. The experimental result is shown in Fig. 20. The PMSM starts up in open loop and switches to sensorless operation at 20 r/min. Then, the speed increases to 200 r/min, in which one step load is added, and then reduced. It can be seen that the estimated speed tracks the actual speed well at steady state and even dynamic process.

C. DC Disturbance Suppression

To further validate the excellent dc elimination performance of second-order SOIFO, the results under dc disturbances, i.e., $\Delta u_\alpha = 5\,\text{V}$ and $\Delta i_\beta = 1.5\,\text{A}$, are given in Figs. 21 and 22, respectively.

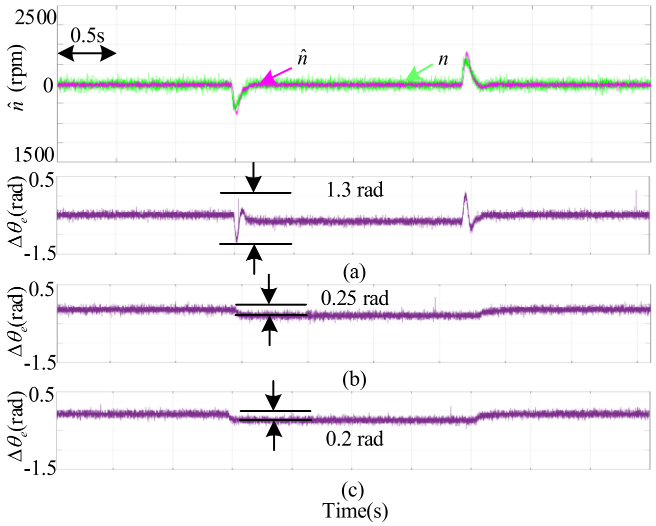

Fig. 19. Experimental comparison of speed and position estimation error with load step disturbance at 2000 r/min. (a) LPF. (b) SOIFO. (c) Second-order SOIFO.

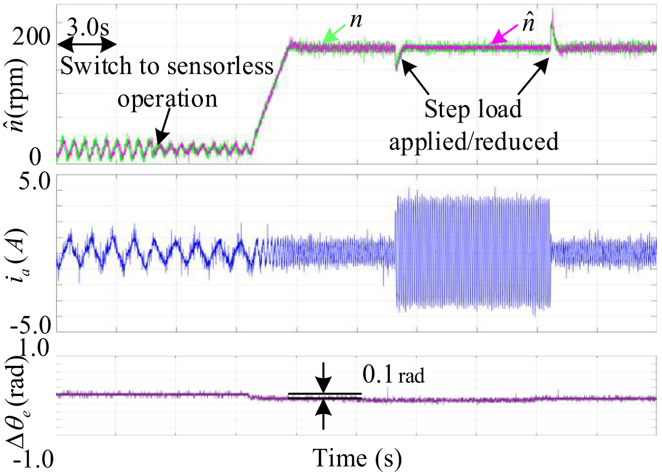

Fig. 20. Experimental result of speed estimation with step load at low-speed region.

In Fig. 21, under the α-axis voltage disturbance, the imbalance 0.05 Wb appears between the estimated α- and β-axis rotor flux linkages by LPF. Meanwhile, the position estimation error fluctuates with 0.65 rad under the dc offset. By SOIFO, the flux estimation imbalance is reduced to 0.03 Wb and the position estimation error oscillation range is 0.25 rad. Fortunately, the rotor flux estimation imbalance and position estimation error do not appear by the help of second-order SOIFO.

The similar situation also happens at the β-axis current disturbance, as shown in Fig. 22. The rotor flux estimation imbalances between the estimated α- and β-axis rotor flux of LPF, SOIFO, and second-order SOIFO are 0.03, 0.017, and 0.005 Wb, respectively. The oscillations of position estimation error of LPF and SOIFO are 0.6 and 0.22 rad, respectively. Fortunately, such kinds of phenomena do not appear in the second-order SOIFO.

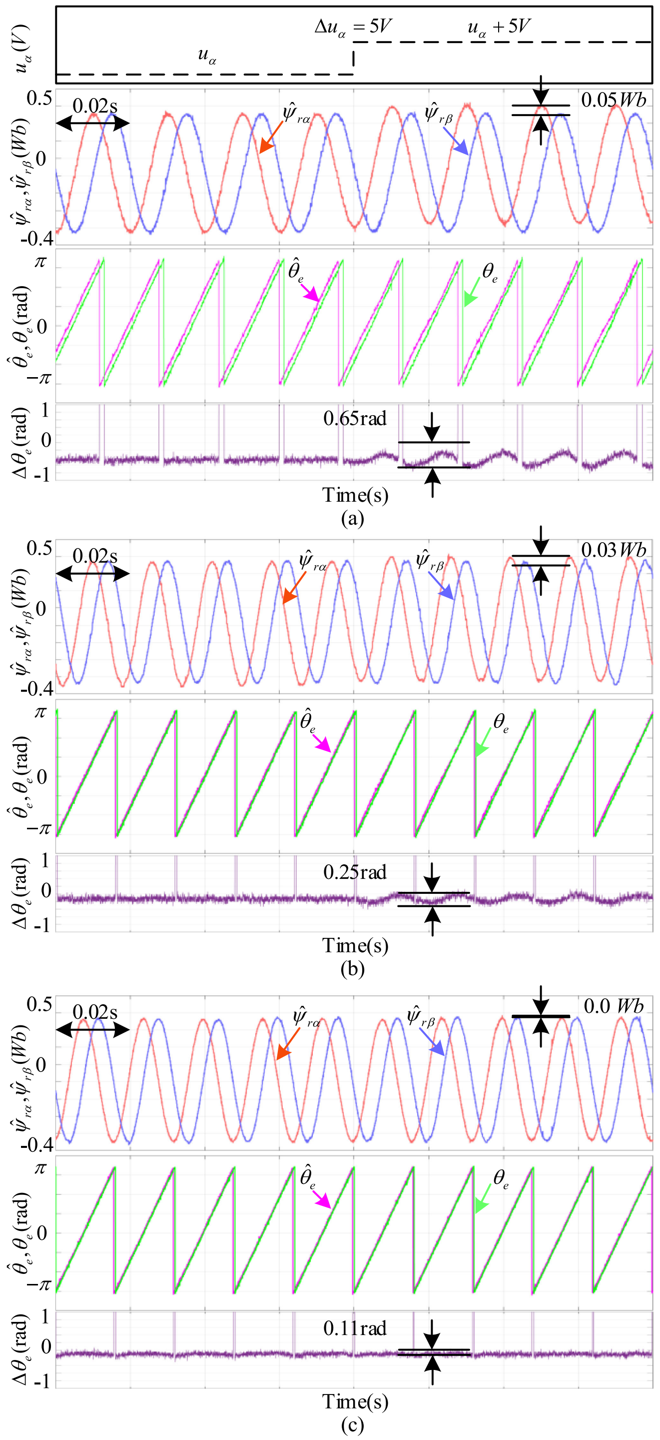

Fig. 21. Estimated rotor flux, rotor position, and errors at 1000 r/min with voltage disturbance ($\Delta u_\alpha = 5$ V). (a) LPF. (b) SOIFO. (c) Second-order SOIFO.

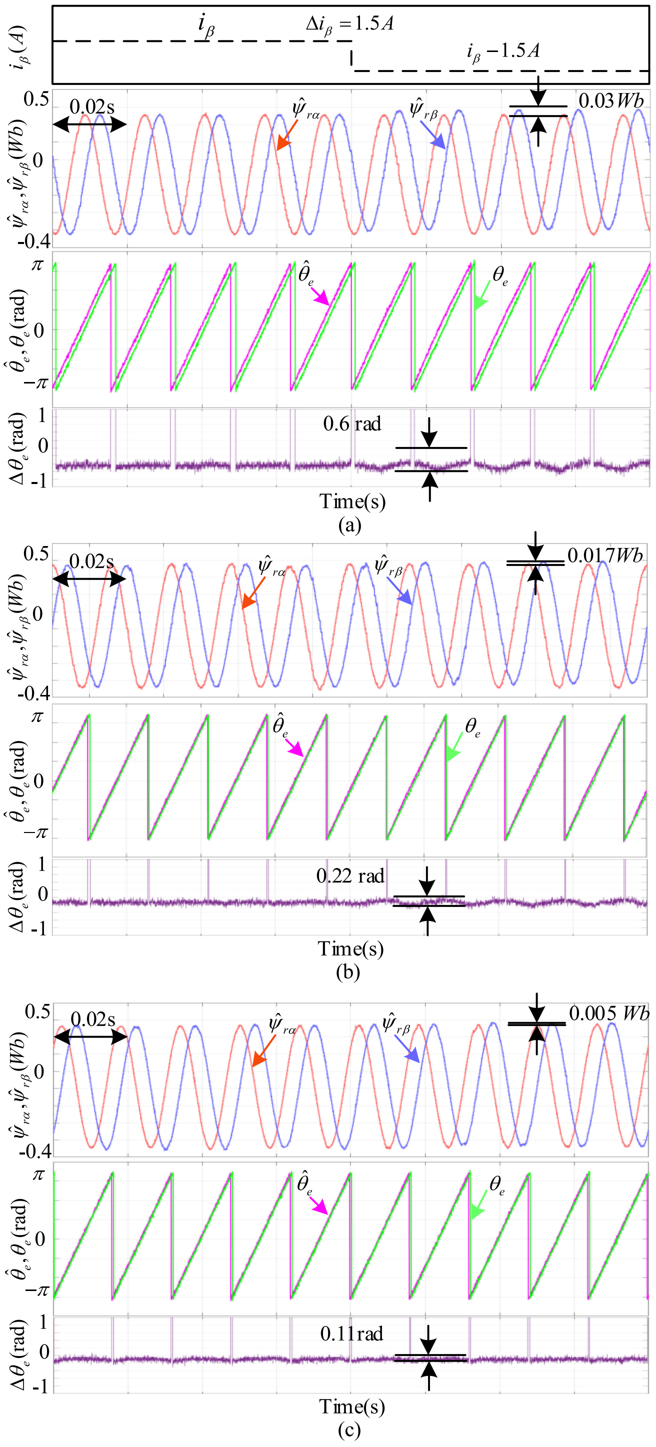

Fig. 22. Estimated rotor flux, rotor position, and errors at 1000 r/min under current disturbance ($\Delta i_\beta = 1.5$ A). (a) LPF. (b) SOIFO. (c) Second-order SOIFO.

Fig. 23 shows the comparisons of observed rotor flux and position based on LPF, SOIFO, and second-order SOIFO with mismatch resistance R_s and 10-N·m load. The resistance is changed from R_{s0} to $0.4R_{s0}$. Because of relatively large current, the resistance mismatch leads to some variations of estimated rotor flux. Generally, the variation will cause the rotor position estimation errors. Fortunately, with strong filtering ability of the proposed flux observer, the estimated rotor position does not fluctuate.

As shown in Figs. 21–23, it can be further concluded that the second-order SOIFO can suppress the position estimation error ripple effectively, and offer strong ability to suppress the dc and harmonics in various operating states.

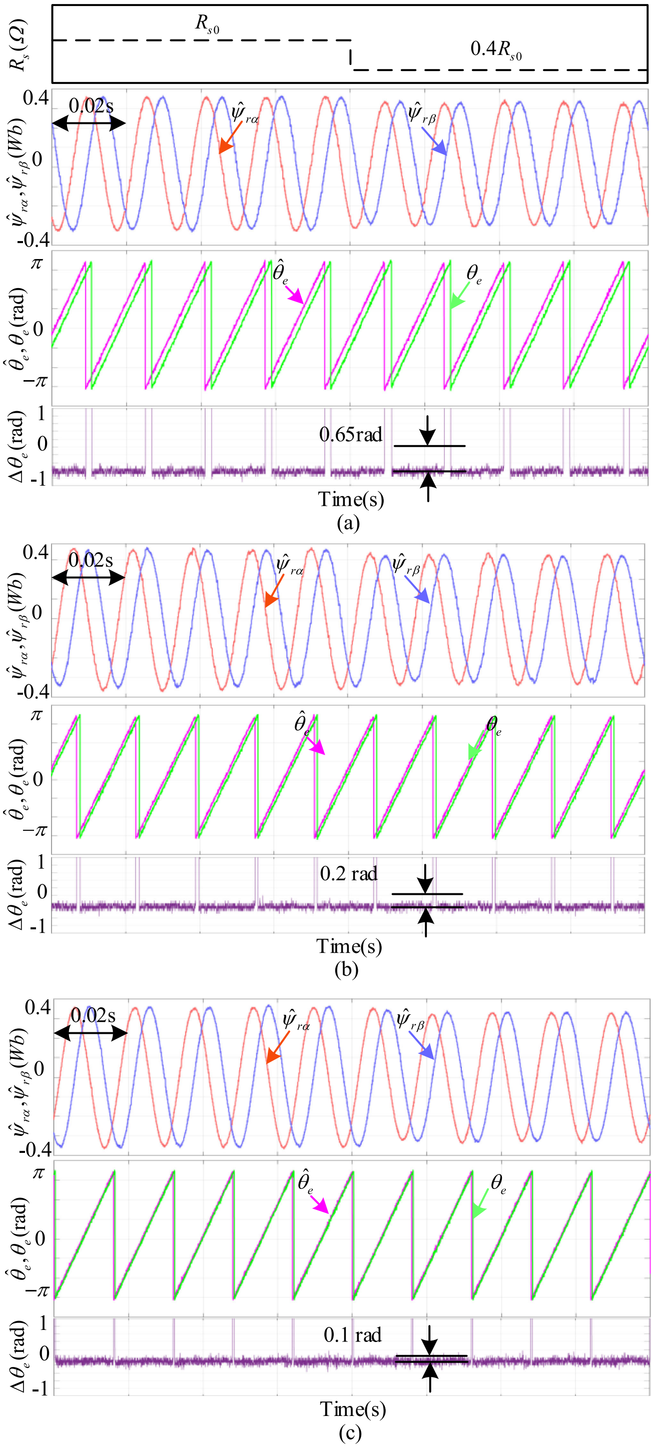

Fig. 23. Estimated rotor flux, position, and rotor position estimation error at 1000 r/min with parameter mismatch ($\Delta R_s = 0.6R_{s0}$). (a) LPF. (b) SOIFO. (c) Second-order SOIFO.

V. CONCLUSION

Two flux observers, SOIFO and second-order SOIFO are proposed in this paper for estimating the rotor flux of PMSM. Compared with the traditional rotor flux observer, the technique can reject the negative effects caused by dc offset and harmonics. Then, the accurate rotor position and speed for sensorless control are calculated by the observed rotor flux. Thereby, the application problems, i.e., parameter mismatches, voltage or current detection errors and unknown integral initial value in the conventional rotor flux observers, are eliminated. The proposed scheme is also easy to implement, and is suitable in low-speed region. Its steady state, dynamic and antidisturbance performances are verified by comprehensive experiments.

TABLE III
SUMMARIZATION OF TRANSFER FUNCTION

Observers	Transfer function
Pure integrator	$1/s$
LPF	$\frac{1}{s+\omega_c}$
SOIFO	$\frac{k\omega'}{s^2+k\omega' s+\omega'^2}$
Second-order SOIFO	$\frac{K_1K_2\omega'^2 s}{s^4+K_2\omega' s^3+(2+K_1K_2)\omega'^2 s^2+K_2\omega'^3 s+\omega'^4}$

APPENDIX

A. *Summarization of the Transfer Function See Table III*

B. *Summarization of the Observed Rotor Flux See Table IV*

C. *Steady-State Rotor Flux Estimation of SOIFO*

1) Analysis of DC Component: Combining (9) and (15), it obtains

$$s\boldsymbol{\Psi}_{r\_\mathrm{SOIFO}}(s) = s\cdot\frac{k\omega'}{s^2+k\omega' s+\omega'^2}\cdot\frac{\boldsymbol{A}_0}{s}. \tag{27}$$

And its pole points can be calculated as

$$p_{\mathrm{SOIFO}1,2} = \frac{k\omega' \pm \omega'\sqrt{k^2-4}}{2}. \tag{28}$$

When $k=\sqrt{2}$, the poles are located in the left half-plane of the complex frequency domain. Therefore, the system is stable. According to the final value theorem of Laplace transform, it can be obtained as

$$\begin{aligned}\lim_{t\to\infty}\boldsymbol{\Psi}_{r\_\mathrm{SOIFO}}(t) &= \lim_{s\to 0} s\boldsymbol{\Psi}_{r\_\mathrm{SOIFO}}(s)\\ &= \lim_{s\to 0} s\cdot\frac{k\omega'}{s^2+k\omega' s+\omega'^2}\cdot\frac{\boldsymbol{A}_0}{s} = \frac{k\boldsymbol{A}_0}{\omega'}.\end{aligned} \tag{29}$$

2) Analysis of Fundamental Component: Combining $s=j\omega'$ with (17), it is written as

$$\frac{k\omega'}{s^2+k\omega' s+\omega'^2} = \frac{1}{j\omega'} = \frac{1}{\omega'}\angle-0.5\pi. \tag{30}$$

Considering the fundamental component of EMF $\boldsymbol{A}_1\sin(\omega_1 t+\varphi_1)$ and $\omega_1=\omega'$, the fundamental component of estimated rotor flux of SOIFO is given as

$$\frac{\boldsymbol{A}_1}{\omega_1}\sin(\omega_1 t+\varphi_1-0.5\pi). \tag{31}$$

TABLE IV
SUMMARIZATION OF THE OBSERVED ROTOR FLUX

Observers	**dc component**	**Fundamental component**	**High-order component**
Pure integrator	$\boldsymbol{A}_o t+\boldsymbol{A}_1\frac{\cos(\varphi_1)}{\omega_1}+\sum\boldsymbol{A}_h\frac{\cos(\varphi_h)}{\omega_h}$	$\frac{\boldsymbol{A}_1}{\omega_1}\sin(\omega_1 t+\varphi_1-0.5\pi)$	$\sum\frac{\boldsymbol{A}_h}{\omega_h}\sin(\omega_h t+\varphi_h-0.5\pi)$
LPF	$\sum\boldsymbol{A}_h\frac{\cos(\varphi_h+\theta_h)}{\sqrt{\omega_h^2+\omega_c^2}}$	$\frac{\boldsymbol{A}_1}{\sqrt{\omega_1^2+\omega_c^2}}\sin(\omega_1 t+\varphi_1-0.5\pi+\theta_1)$	$\sum\frac{\boldsymbol{A}_h}{\sqrt{\omega_h^2+\omega_c^2}}\sin(\omega_h t+\varphi_h-0.5\pi+\theta_h)$
SOIFO	$\frac{\boldsymbol{A}_o k}{\omega_1}$	$\frac{\boldsymbol{A}_1}{\omega_1}\sin(\omega_1 t+\varphi_1-0.5\pi)$	$\sum\frac{1}{\sqrt{(1-h^2)^2/k^2h^2+1}}\cdot\frac{\boldsymbol{A}_h}{\omega_h}\sin(\omega_h t+\varphi_h-0.5\pi+\gamma_{h1})$
Second-order SOIFO	0	$\frac{\boldsymbol{A}_1}{\omega_1}\sin(\omega_1 t+\varphi_1-0.5\pi)$	$\sum\frac{1}{\sqrt{\frac{[1-h^2(2+K_1K_2)+h^4]^2}{(h^2K_1K_2)^2}+\frac{(hK_2-h^3K_2)^2}{(h^2K_1K_2)^2}}}\frac{\boldsymbol{A}_h}{\omega_h}\sin(\omega_h t+\varphi_h-0.5\pi+\gamma_{h2})$

3) Analysis of Harmonics: Combining $s=j\omega_h=jh\omega'$ with (15), it is written as

$$\frac{k\omega'}{s^2+k\omega' s+\omega'^2}=\frac{k\omega'}{-h^2\omega'^2+\omega'^2+jhk\omega'^2}=\frac{1}{\sqrt{(1-h^2)^2+h^2k^2}}\frac{k}{\omega'}\angle\theta_1 \tag{32}$$

where $\theta_1=\tan^{-1}(\frac{k\omega'\omega_h}{\omega_h^2-\omega'^2})$. Considering the harmonics of back EMF $\sum\boldsymbol{A}_h\sin(\omega_h t+\varphi_h)$, the high-order component of estimated rotor flux linkage of SOIFO is given as

$$\sum\frac{1}{\sqrt{(1-h^2)^2+h^2k^2}}\frac{\boldsymbol{A}_h k}{\omega'}\angle\omega_h t+\varphi_h+\theta_h$$
$$=\sum\frac{1}{\sqrt{(1-h^2)^2/k^2h^2+1}}\cdot\frac{\boldsymbol{A}_h}{\omega_h}\sin(\omega_h t+\varphi_h-0.5\pi+\gamma_{h1}) \tag{33}$$

where $\gamma_{h1}=\tan^{-1}(\frac{\omega'^2-\omega_h^2}{k\omega'\omega_h})$. Ultimately, the steady-state rotor flux linkage of SOIFO is described as

$$\boldsymbol{\Psi}_{r\_\text{SOIFO}}(t)=\frac{\boldsymbol{A}_o k}{\omega_1}+\frac{\boldsymbol{A}_1}{\omega_1}\sin(\omega_1 t+\varphi_1-0.5\pi)$$
$$+\sum\frac{1}{\sqrt{(1-h^2)^2/k^2h^2+1}}\cdot\frac{\boldsymbol{A}_h}{\omega_h}\sin(\omega_h t+\varphi_h-0.5\pi+\gamma_h). \tag{34}$$

D. Steady-State Rotor Flux Estimation of Second-Order SOIFO

1) Analysis of DC Component: Combining (9) and (20), it obtains

$$s\boldsymbol{\Psi}_{r\_\text{SOSOIFO}}(s)$$
$$=s\frac{K_1K_2\omega'^2 s}{s^4+K_2\omega' s^3+(2+K_1K_2)\omega'^2 s^2+K_2\omega'^3 s+\omega'^4}\frac{\boldsymbol{A}_0}{s}. \tag{35}$$

It can be concluded that the poles are located in the left half-plane of the complex frequency domain. Thus, the final value theorem of Laplace transform can be used as

$$\lim_{t\to\infty}\boldsymbol{\Psi}_{r\_\text{SOSOIFO}}(t)=\lim_{s\to 0}s\boldsymbol{\Psi}_{r\_\text{SOSOIFO}}(s)$$
$$=\lim_{s\to 0}s\cdot\frac{K_1K_2\omega'^2 s}{s^4+K_2\omega' s^3+(2+K_1K_2)\omega'^2 s^2+K_2\omega'^3 s+\omega'^4}$$
$$\cdot\frac{\boldsymbol{A}_0}{s}=0. \tag{36}$$

2) Analysis of Fundamental Component: Combining $s=j\omega'$ and (20), it is written as

$$\frac{K_1K_2\omega'^2 s}{s^4+K_2\omega' s^3+(2+K_1K_2)\omega'^2 s^2+K_2\omega'^3 s+\omega'^4}$$
$$=\frac{1}{j\omega'}=\frac{1}{\omega'}\angle-0.5\pi. \tag{37}$$

Considering the fundamental component of EMF $\boldsymbol{A}_1\sin(\omega_1 t+\varphi_1)$ and $\omega_1=\omega'$, the fundamental component of estimated rotor flux linkage is given as

$$\frac{\boldsymbol{A}_1}{\omega_1}\sin(\omega_1 t+\varphi_1-0.5\pi). \tag{38}$$

3) Analysis of Harmonics: Combining $s=j\omega_h=jh\omega'$ with (20), it is written as

$$\frac{K_1K_2\omega'^2 s}{s^4+K_2\omega' s^3+(2+K_1K_2)\omega'^2 s^2+K_2\omega'^3 s+\omega'^4}$$
$$=\frac{jK_1K_2\omega'^3}{h^4\omega'^4-jh^3K_2\omega'^4-h^2(2+K_1K_2)\omega'^4+jhK_2\omega'^4+\omega'^4}$$
$$=\frac{hK_2-h^3K_2+j[1-h^2(2+K_1K_2)+h^4]}{[1-h^2(2+K_1K_2)+h^4]^2+(hK_2-h^3K_2)^2}\frac{hK_1K_2}{\omega'}$$
$$=\frac{1}{\sqrt{[1-h^2(2+K_1K_2)+h^4]^2+(hK_2-h^3K_2)^2}}\frac{hK_1K_2}{\omega'}\angle\theta_2 \tag{39}$$

where $\theta_2=\tan^{-1}(\frac{\omega'^4-h^2(2+K_1K_2)\omega'^2\omega_h^2+\omega_h^4}{K_2\omega'^3\omega_h-K_2\omega'\omega_h^3})$. Considering the harmonics of back EMF $\sum\boldsymbol{A}_h\sin(\omega_h t+\varphi_h)$, the high-order component of estimated rotor flux linkage of second-order

SOIFO is given as

$$\begin{aligned}
&\sum \frac{1}{\sqrt{\left[1-h^2(2+K_1K_2)+h^4\right]^2+\left(hK_2-h^3K_2\right)^2}}\\
&\quad\cdot \frac{hK_1K_2}{\omega'}\angle\theta_2 \cdot \sum \boldsymbol{A}_h \sin\left(\omega_h t+\varphi_h\right)\\
&=\sum \frac{1}{\sqrt{\frac{\left[1-h^2(2+K_1K_2)+h^4\right]^2}{\left(h^2K_1K_2\right)^2}+\frac{\left(hK_2-h^3K_2\right)^2}{\left(h^2K_1K_2\right)^2}}}\\
&\quad\cdot \frac{\boldsymbol{A}_h}{\omega_h}\angle\omega_h t+\varphi_h+\theta_2\\
&=\sum \frac{1}{\sqrt{\frac{\left[1-h^2(2+K_1K_2)+h^4\right]^2}{\left(h^2K_1K_2\right)^2}+\frac{\left(hK_2-h^3K_2\right)^2}{\left(h^2K_1K_2\right)^2}}}\\
&\quad\cdot \frac{\boldsymbol{A}_h}{\omega_h}\sin\left(\omega_h t+\varphi_h-0.5\pi+\gamma_{h2}\right)
\end{aligned} \tag{40}$$

where $\gamma_{h2}=\tan^{-1}\left(\frac{K_2\omega'\omega_h^3-K_2\omega'^3\omega_h}{\omega'^4-h^2(2+K_1K_2)\omega'^2\omega_h^2+\omega_h^4}\right)$. The steady-state rotor flux of second-order SOIFO is described as

$$\begin{aligned}
\boldsymbol{\Psi}_{r\_\mathrm{SOSOIFO}}(t) &= \frac{\boldsymbol{A}_1}{\omega_1}\sin\left(\omega_1 t+\varphi_1-0.5\pi\right)\\
&\quad+\sum \frac{1}{\sqrt{\frac{\left[1-h^2(2+K_1K_2)+h^4\right]^2}{\left(h^2K_1K_2\right)^2}+\frac{\left(hK_2-h^3K_2\right)^2}{\left(h^2K_1K_2\right)^2}}}\\
&\quad\cdot \frac{\boldsymbol{A}_h}{\omega_h}\sin\left(\omega_h t+\varphi_h-0.5\pi+\gamma_{h2}\right).
\end{aligned} \tag{41}$$

REFERENCES

[1] S. Bolognani, R. Oboe, and M. Zigliotto, “Sensorless full-digital PMSM drive with EKF estimation of speed and rotor position,” *IEEE Trans. Ind. Electron.*, vol. 46, no. 1, pp. 184–191, Feb. 1999.

[2] J. Solsona, M. I. Valla, and C. Muravchik, “Nonlinear control of a permanent magnet synchronous motor with disturbance torque estimation,” *IEEE Trans. Energy Convers.*, vol. 15, no. 2, pp. 163–168, Jun. 2000.

[3] S. Morimoto, K. Kawamoto, and M. Sanada, “Sensorless control strategy for salient-pole PMSM based on extended EMF in rotating reference frame,” *IEEE Trans. Ind. Appl.*, vol. 38, no. 4, pp. 1054–1061, Jul. 2002.

[4] Y. Jiang, W. Xu, and C. Mu, “Improved deadbeat predictive current control combined sliding mode strategy for PMSM drive system,” *IEEE Trans. Veh. Technol.*, vol. 67, no. 1, pp. 251–263, Jan. 2018.

[5] S. Yang, S. M. Yang, and J. H. Hu, “Design consideration on the square-wave voltage injection for sensorless drive of interior permanent-magnet machines,” *IEEE Trans. Ind. Electron.*, vol. 64, no. 1, pp. 159–168, Jan. 2017.

[6] A. H. Almarhoon, Z. Q. Zhu, and P. Xu, “Improved pulsating signal injection using zero-sequence carrier voltage for sensorless control of dual three-phase PMSM,” *IEEE Trans. Energy Convers.*, vol. 32, no. 2, pp. 436–446, Jun. 2017.

[7] S. C. Yang, S. M. Yang, and J. H. Hu, “Design consideration of interior permanent magnet machine position sensorless drive using square-wave voltage injection,” in *Proc. Int. Conf. Energy Convers. Congr. Expo.*, Feb. 2015, pp. 1–6.

[8] R. Dhaouadi, N. Mohan, and L. Norum, “Design and implementation of an extended kalman filter for the state estimation of a permanent magnet synchronous motor,” *IEEE Trans. Power Electron.*, vol. 6, no. 3, pp. 491–497, Jul. 1991.

[9] X. Song, J. Fang, and B. Han, “Adaptive compensation method for high-speed surface PMSM sensorless drives of EMF-based position estimation error,” *IEEE Trans. Power Electron.*, vol. 31, no. 2, pp. 1438–1449, Feb. 2016.

[10] G. Wang, Z. Li, and G. Zhang, “Quadrature PLL-based high-order sliding-mode observer for IPMSM sensorless control with online MTPA control strategy,” *IEEE Trans. Energy Convers.*, vol. 28, no. 1, pp. 214–224, Mar. 2013.

[11] S. Diao, D. Diallo, and Z. Makni, “A differential algebraic estimator for sensorless permanent-magnet synchronous machine drive,” *IEEE Trans. Energy Convers.*, vol. 30, no. 1, pp. 82–89, Mar. 2015.

[12] J. Lee, J. Hong, and K. Nam, “Sensorless control of surface-mount permanent-magnet synchronous motors based on a nonlinear observer,” *IEEE Trans. Power Electron.*, vol. 25, no. 2, pp. 290–297, Feb. 2010.

[13] J. Choi, K. Nam, and A. A. Bobtsov, “Robust adaptive sensorless control for permanent-magnet synchronous motors,” *IEEE Trans. Power Electron.*, vol. 32, no. 5, pp. 3989–3997, May 2017.

[14] G. Feng, C. Lai, and K. Mukherjee, “Online PMSM magnet flux estimation for rotor magnet condition monitoring using harmonics in speed measurements,” *IEEE Trans. Ind. Appl.*, vol. 53, no. 3, pp. 2786–2794, Feb. 2017.

[15] A. Bobtsov, A. Pyrkin, and R. Ortega, “A robust globally convergent position observer for the permanent magnet synchronous motor,” *Automatica*, vol. 61, pp. 47–54, Nov. 2015.

[16] R. Ortega, L. Praly, and A. Astolfi, “Estimation of rotor position and speed of permanent magnet synchronous motors with guaranteed stability,” *IEEE Trans. Control Syst. Technol.*, vol. 19, no. 3, pp. 601–614, May 2011.

[17] S. Po-ngam and S. Sangwongwanich, “Stability and dynamic performance improvement of adaptive full-order observers for sensorless PMSM drive,” *IEEE Trans. Power Electron.*, vol. 27, no. 2, pp. 588–600, Feb. 2012.

[18] Y. Park and S.-K. Sul, “Sensorless control method for PMSM based on frequency-adaptive disturbance observer,” *IEEE J. Emerg. Sel. Topics Power Electron.*, vol. 2, no. 2, pp. 143–151, Jun. 2014.

[19] M. Hinkkanen, T. Tuovinen, and L. Harnefors, “A combined position and stator-resistance observer for salient PMSM drives: Design and stability analysis,” *IEEE Trans. Power Electron.*, vol. 27, no. 2, pp. 601–609, Feb. 2012.

[20] M. Ciobotaru, R. Teodorescu, and F. Blaabjerg, “A new single-phase PLL structure based on second order generalized integrator,” in *Proc. IEEE Power Electron. Spec. Conf.*, Jun. 2006, pp. 1–7.

[21] Z. Xin, X. Wang, Z. Qin, M. Lu, P. C. Loh, and F. Blaabjerg, “An improved second-order generalized integrator based quadrature signal generator,” *IEEE Trans. Power Electron.*, vol. 31, no. 12, pp. 8068–8073, Dec. 2016.

[22] R. Zhao, Z. Xin, and P. C. Loh, “A novel flux estimator based on multiple second-order generalized integrators and frequency-locked loop for induction motor drives,” *IEEE Trans. Power Electron.*, vol. 32, no. 8, pp. 6286–6296, Aug. 2017.

[23] P. Rodriguez, A. Luna, and I. Candela, “Multi-resonant frequency-locked loop for grid synchronization of power converters under distorted grid conditions,” *IEEE Trans. Ind. Electron.*, vol. 58, no. 1, pp. 127–138, Jan. 2011.

Wei Xu (M’09–SM’13) received the B.E. and M.E. degrees from Tianjin University, Tianjin, China, in 2002 and 2005, respectively, and the Ph.D. degree from the Chinese Academy of Sciences, Beijing, China, in 2008, all in electrical engineering.

From 2008 to 2012, he held several academic positions with Australian and Japanese universities and companies. Since 2013, he has been a Full Professor with the State Key Laboratory of Advanced Electromagnetic Engineering and Technology, School of Electrical and Electronic Engineering, Huazhong University of Science and Technology, Wuhan, China. His research interests mainly include the electromagnetic design and control algorithms of linear/rotary machines, including induction, permanent magnets, switched reluctance, and other emerging novel structure machines.

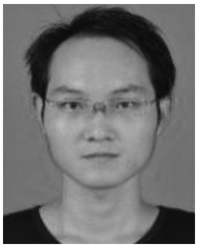

Yajie Jiang received the B.S. degree in electrical engineering from Zhengzhou University, Zhengzhou, China, in 2015. He is currently working toward the M.S. degree in the School of Electrical and Electronic Engineering, Huazhong University of Science and Technology, Wuhan.

His research interests include advanced control methods for power electronics.

Chaoxu Mu (M'15) received the Ph.D. degree in control science and engineering from Southeast University, Nanjing, China, in 2012.

She was a Visiting Ph.D. Student with the Royal Melbourne Institute of Technology University, Melbourne, Australia, from October 2010 to November 2011, and was a Postdoctoral Fellow with the Department of Electrical, Computer and Biomedical Engineering, University of Rhode Island, Kingston, RI, USA, from December 2014 to August 2016. She is currently an Associate Professor with the School of Electrical and Information Engineering, Tianjin University, Tianjin, China. Her current research interests include nonlinear system control and optimization, and adaptive and learning systems.

Frede Blaabjerg (S'86–M'88–SM'97–F'03) received the Ph.D. degree in electrical engineering from Aalborg University, Aalborg, Denmark, in 1995.

He was with ABB-Scandia, Randers, Denmark, from 1987 to 1988. At Aalborg University, he became an Assistant Professor in 1992, an Associate Professor in 1996, and a Full Professor of power electronics and drives in 1998. From 2017, he became a Villum Investigator. He has authored or coauthored more than 450 journal papers in the fields of power electronics and its applications. He is the Coauthor of two monographs and an Editor of six books in power electronics and its applications. His current research interests include power electronics and its applications such as in wind turbines, photovoltaic systems, reliability, harmonics and adjustable speed drives.

Dr. Blaabjerg was the Editor-in-Chief for the IEEE TRANSACTIONS ON POWER ELECTRONICS from 2006 to 2012. He was the Distinguished Lecturer for the IEEE Power Electronics Society (PELS) from 2005 to 2007 and for the IEEE Industry Applications Society from 2010 to 2011 as well as 2017 to 2018. He was nominated in 2014, 2015, 2016, and 2017 by Thomson Reuters to be among the most 250 cited researchers in Engineering in the world. In 2017, he became Honoris Causa at the University Politehnica Timisoara, Romania. He was recipient of 24 IEEE Prize Paper Awards, the IEEE PELS Distinguished Service Award in 2009, the EPE-Power Electronics and Motion Control (PEMC) Council Award in 2010, the IEEE William E. Newell Power Electronics Award 2014, and the Villum Kann Rasmussen Research Award 2014.